applied sciences

Article

Experimental Study on a Granular Material-Filled Lining in a High Ground-Stress Soft-Rock Tunnel

Jie Liu [1,2], Bin Wang [1,2,*], Yansong Wang [1,2], Lei Shi [1,2], Xiaokang Xie [1,2] and Jun Lan [1,2]

[1] College of Civil Engineering & Architecture, China Three Gorges University, Yichang 443002, China; 532128197907070015@ctgu.edu.cn (Jie Liu)
[2] Key Laboratory of Geological Hazards on Three Gorges Reservoir Area, Ministry of Education, China Three Gorges University, Yichang 443002, China
* Correspondence: 202108140011007@ctgu.edu.cn; Tel.: +86-18739954385

Featured Application: Yielding- and relief-pressure support technology of a lining filled with granular material is proposed. This technology will guide the design and construction of tunnel projects' supporting structures in the future.

Abstract: For high ground-stress soft-rock tunnels surrounding rock with large deformation, rapid deformation rate, a long creep time, and a high likelihood of to causing initial and secondary lining damage, the yielding and relief-pressure support technology of a lining filled with a granular material is proposed. A layer of granular material is placed at the reserved deformation layer of the tunnel to provide the surrounding rock with a certain amount of deformation space. Confined compression tests were undertaken to study the laws of compressive strain, load reduction law, and horizontal force variation of different granular materials under different rock stresses. The research showed that the compressibility and load reduction performance of 8 mm soil was optimal. Its maximum compressive strain reached 47.6%, and the total load reduction rate reached 71%. The yielding- and relief-pressure effects of the granular sand-filled lining support were analyzed from the angles of deflection, pressure, and energy. The results show that the highest reduction rate of deflection was 36.7%, and the greatest load reduction rate of pressure was 78%. The grainy filling material can remove part of the load imposed by the surrounding rock on the support structure of the secondary lining through yielding pressure and relief pressure, which dramatically reduces the damage to the secondary lining from the surrounding rock. The research results have specific reference significance for designing and constructing tunnel support structures.

Keywords: high ground stress; soft-rock tunnel; granular material-filled lining; yielding-pressure support; relief-pressure support

check for updates

Citation: Liu, J.; Wang, B.; Wang, Y.; Shi, L.; Xie, X.; Lan, J. Experimental Study on a Granular Material-Filled Lining in a High Ground-Stress Soft-Rock Tunnel. *Appl. Sci.* **2023**, *13*, 13326. https://doi.org/10.3390/app132413326

Academic Editors: Giuseppe Lacidogna and Asterios Bakolas

Received: 28 October 2023
Revised: 4 December 2023
Accepted: 13 December 2023
Published: 17 December 2023

1. Introduction

The scale and depth of underground projects in the nuclear, national defense, transportation, and water conservation industries have proliferated in recent years. Although underground engineering has developed rapidly, there are also enormous challenges to be faced. The deformation and destruction of deep, high ground-stress soft-rock chambers present several technical challenges, such as long creep times, large creep volumes, and rapid deformation rates. In response to this significant problem, national and international scholars have developed novel support concepts and conducted helpful research. Kang Hongpu et al. [1] proposed the theory and technology of high prestressing and strong support to significantly increase the stiffness and strength of the initial support and carried out extensive field tests in the kilometer-deep shaft roadway of the Xinwen Mine. Zhou Yi et al. [2] concluded that the solution of higher support strength and stiffness has the maximum support effect. Xie Shengrong et al. [3] proposed an intensive, high-strength reinforced arch in one anchor spray injection to strengthen pressure arch support technology.

In addition, many practical projects have also adopted the "strong support and rigid top" support method [4–8] to improve the lining structure's safety by increasing the strength and stiffness of the support.

Substantial engineering practice worldwide has shown that in the case of high ground-stress soft-rock tunnels surrounding rock deformation, increasing the strength and stiffness of the support structure alone cannot effectively solve the problem, and that this approach is likely to lead to support structure damage or instability, such as the concrete spray layer falling off, anchor rod destabilization, steel bracket bending, and other phenomena [9–11]. The deformation of the surrounding rock is usually controlled to some extent after several cycles of support, rupture, and replacement. However, there are more significant safety risks during construction, with increasing construction costs. In recent years, some researchers have assessed the time-dependent stability of the tunnel's permanent lining. Xu et al. [12] investigated the weak rock creep behavior in the failure process of the final lining of the Dujia mountain tunnel. Xu et al. [13] investigated the transversely isotropic creep behavior of phyllite and its influence on the long-term safety of the secondary lining of tunnels. Xu and Gutierrez [14] studied the damage evolution of the final tunnel lining under the combined effects of corrosion of the temporary support and the creep behavior of the surrounding rock.

With the gradual maturity of the New Austrian Tunnelling Method, based on the principle of "rigidity and flexibility", scholars have improved some construction methods for soft-rock cave support. Yielding-pressure support has been widely researched and applied in high ground-stress soft-rock large-deformation tunnels [15–20]. Sun Jun [21] believes that for underground caverns with large deformations in soft rock, the support structure should have "strong flexibility, high shrink ability, supporting while flexible, [and] economy and convenience of construction". Scholars worldwide have proposed a support type that can realize the function of "supporting while yielding" through the yielding-pressure anchor rod and retractable steel frame [22–27]. This can produce a degree of deformation under the condition of providing constant support resistance to guarantee the support structure's safety. Chen Weizhong and G. Barla [28,29] proposed that concrete with high compressibility and superior ductility can be well adapted to the creep deformation of the surrounding rock as a reserved deformation layer filling material for deeply buried soft-rock tunnels. Tian Yun et al. [30] considered the time-dependent weakening characteristic of weak surrounding rock strength in compressible layer design. Scholars have conducted in-depth research into the different filling materials of compressible layers. Wu K et al. [31] considered foamed concrete the most promising filling material for compressible layers. Hu Xiongyu et al. [9,10] presented a compressible ceramsite layer behind the pipe-sheet lining wall to achieve yielding. Zheng Pengqiang et al. [32] proposed a support technology solution combining dynamic pressure relief and active pressure in U-shaped steel-reinforced brackets and foam concrete filling combined with prestressing anchor cables.

Yielding capacity is limited if a compressible layer is applied to achieve yielding support. After a certain compression level, it is more challenging for the lining structure to continue to exert pressure. If the lining structure stress is not released in time, it increases, and the support effect is unsatisfactory. A U-shaped shrinkable steel bracket prevents warpage damage to the steel arch by allowing movable joints to slide and cause shrinkage of the steel arch section. However, the clamping force of the sliding joints is not large enough to provide support resistance in the initial support of the steel arch. If the clamping force is too high, then it will not work when the steel arch is damaged. Some researchers [33–36] have also conducted numerical simulations related to yielding-pressure support for tunnel lining.

The above research shows that rigid support technology is used more for point or line reinforcement, emphasizing solid support and sturdy top. However, this is inadequate for supporting high ground-stress soft rocks with large deformations over long periods. Existing flexible support technology can only create controllable support forces in point or line form. However, it cannot produce controllable and homogenized surface support within a wide range of free faces. Based on this, we propose a lining filled with granular material, which provides yielding-pressure and relief-pressure support technology with a compressible buffer layer at the reserved deformation layer. Granular material mobility forms a controllable and homogenized surface support force. The compressibility of the filling material absorbs the pressure generated by the deformation of the surrounding rock, which reduces the yielding pressure. Using the automatic discharge of granular material releases the surrounding rock pressure, which has a better pressure relief effect so that the load on the lining structure is no greater than the set threshold. Therefore, the safety and stability of the lining structure can be guaranteed through the yielding pressure and relief pressure of the lining. This technology provides an innovative way to support soft-rock tunnels with high ground stress.

2. Principle of a Lining with Compressible Granular Filling Material

2.1. Technical Stage of the Lining Support with Compressible Granular Filling Material

The specific method of granular material-filled lining support technology is to place a buffer layer of filling material (ceramsite, soil, sand) with good mobility and compressibility at the reserved deformation layer between the tunnel's surrounding rock and the secondary lining [31,37], and to place a pressure relief valve with a threshold in the lining structure. The buffer layer can provide deformation space for the adjacent rock when the surrounding rock is deformed by taking advantage of the mobility, compressibility, and discharge performance of the granular material. It can also absorb part of the surrounding rock stress due to its strength, so that the stress of the secondary tunnel lining support structure is more uniform and better able to protect the overall tunnel support structure. After tunnel excavation, the granular material filling layer is installed directly between the tunnel's surrounding rock and secondary lining. Following this, in the area with significant stress, deep anchors are implanted for local reinforcement and support. This method can negate the need for part of the initial lining anchor bolt support and reduce the free time of the tunnel's excavated surface to effectively restrain the displacement of the free surface and the development of the plastic zone towards the depth of the surrounding rock.

The granular material-filled lining support process is divided into three stages, as shown in Figure 1.

Filling lining initial installation stage: The reserved deformation layer of the tunnel is filled with the compressible granular filling material, automatic pressure relief valves are installed on both sides of the arch feet and on the top of the arch, and the pressure relief threshold P3, which can be adjusted, is set. At this stage, the supporting structure's stress distribution is not uniform, and its stress is less than P1, as shown in Figure 1a.

Homogenization and pressurization stage below the relief-pressure threshold: With the development of the deformation of the surrounding rock, granular materials flow, compress, and break. The force pattern of the lining structure is changed from a point type to a surface type. At this point, the force on the support structure increases to P2, as shown in Figure 1b.

Automatic pressure-relief stage of the lining: When the pressure in the granular material-filled lining reaches the pressure relief threshold P3 and the filling materials release through the automatic pressure relief valves, the pressure of the supporting structure is maintained at P3 without further increase. The lining structure is evenly forced, as shown in Figure 1c.

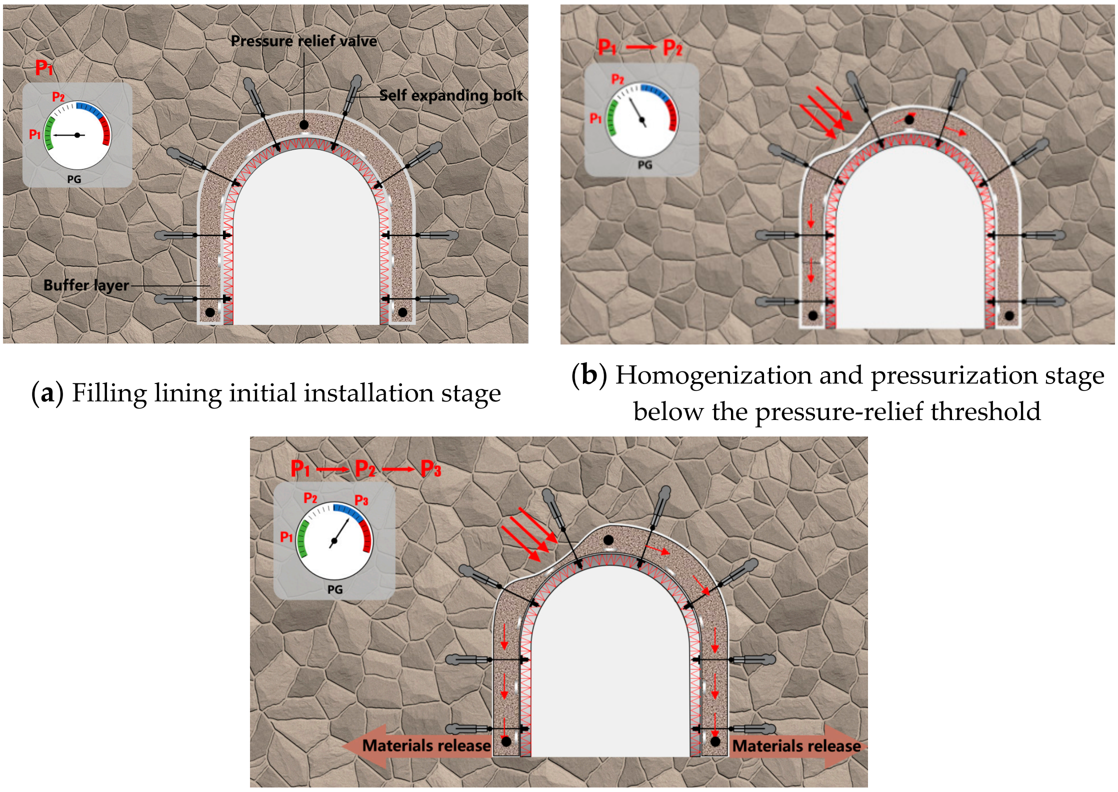

(**a**) Filling lining initial installation stage

(**b**) Homogenization and pressurization stage below the pressure-relief threshold

(**c**) Automatic pressure-relief stage of the lining

Figure 1. The granular material-filled lining support stage.

2.2. Technical Characteristics of the Compressible Granular Filling Lining Support

Based on the above overview of granular material-filled lining technology, the technical characteristics of the proposed lining support and traditional support are compared and analyzed, as shown in Figure 2.

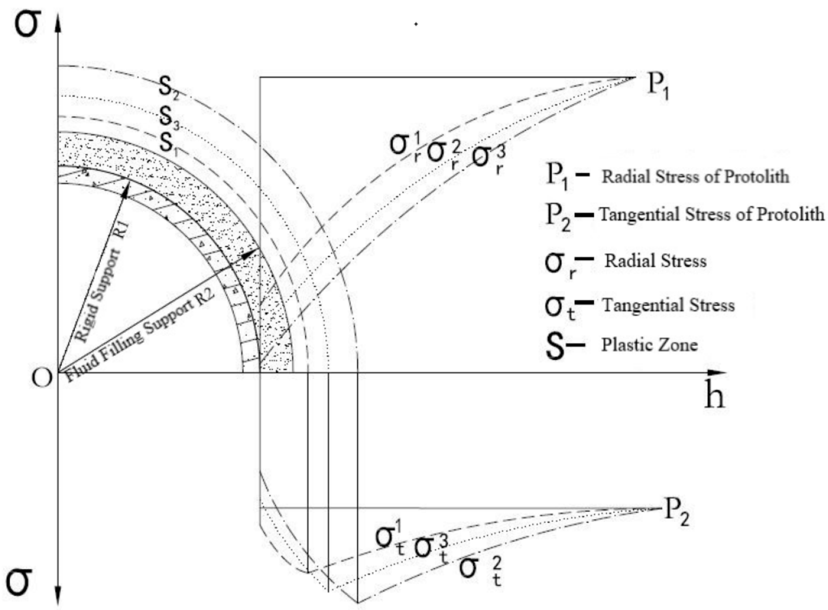

Figure 2. Principle of the compressible granular filling lining support. Note: In the figure, mark 1 represents the rigid support, mark 2 represents the yielding support, and mark 3 represents the compressible granular filling lining support.

2.2.1. Comparative Analysis of the Plastic Zone of the Granular Filling Lining

The plastic zone radius R comprises two parts: the radius Δr of plastic zone development before support and after excavation, and the radius r of plastic zone development after support. As shown in Equations (1) and (2):

$$R = \Delta r + r \tag{1}$$

$$r = r_0 \left[(1 - sin\varphi) \frac{c\ cot\varphi + \sigma_z}{c\ cot\varphi + P_\alpha} \right]^{\frac{1-sin\varphi}{2sin\varphi}} \tag{2}$$

where r_0 is the tunnel's excavation radius, φ is the angle of internal friction, c is cohesion, σ_z is initial ground stress, and P_α is the horizontal support reaction force. For the same tunnel, only Δr and P_α are different.

The compressible granular filling lining is used as a secondary lining immediately after tunnel excavation. The surrounding rock's free time is $T_3 \ll T_2 \approx T_1$; therefore, $\Delta r_1 \approx \Delta r_2 >> \Delta r_3 \approx 0$. The granular material filling lining can provide a uniform, controllable surface support force in time. It can reduce stress concentration, avoid plastic zone overdevelopment, and make $P_{\alpha_2} < P_{\alpha_3} < P_{\alpha_1}$; thus, $r_1 < r_3 < r_2$, and the radius of the plastic zone is between that of traditional support and yielding support.

2.2.2. Comparative Analysis of the Tangential Forces

(1) The plastic zone has a load-reduction effect η_1 due to the surrounding rock cracking and loosening. Figure 2 shows the tangential force $\sigma_t^1 < \sigma_t^3 < \sigma_t^2$.

(2) The longer the distance is from the plastic zone, the less the load-reduction effect η_1. The tangential force increases constantly. There is no cracking or load-reduction effect η_1 at the plastic zone and elastic zone interface. The elastic region has an inward-moving loading effect η_2, and the tangential force peaks here. The larger the plastic zone is, the greater the loading effect η_2 is and the greater the tangential force peak value is, i.e., $\sigma_t^2 > \sigma_t^3 > \sigma_t^1$.

(3) Deep into the surrounding rock, the load-reduction effect η_2 decreases, and the tangential force drops to the original rock stress σ_t^1, σ_t^2, and σ_t^3 at a certain depth.

2.2.3. Comparative Analysis of the Radial Force

The lining support filled with granular material can provide timely surface support force and homogenize surrounding rock pressure. The compression crushing and discharge of the compressible granular filling material can reduce the benefit of radial force. This can minimize the radial force of the compressible granular filling lining, therefore, $\sigma_r^1 > \sigma_r^2 > \sigma_r^3$.

3. Granular Filling Materials and Test Methods

3.1. Granular Filling Materials

Based on the granular material-filled lining support principle, a unit body was selected for a confined compression test. The support reaction force, maximum settlement, deformation settlement law, and supporting effect of compressible granular filling materials (sand, soil, and ceramsite) in a tunnel with surrounding rock deformation were studied.

Based on the above principles, the filling materials were required to ① provide a certain amount of deformation space for the surrounding rock; ② homogenize the lining forces during the surrounding rock creep; ③ significantly decrease the expansion of the plastic zone during the creep process of the surrounding rock so that the final creep variable of the surrounding rock is significantly reduced; ④ reduce overall construction cost and other requirements; and ⑤ combine previous research on granular filling materials conducted by the team members. Therefore, the materials selected in this paper were as follows:

Sand with excellent fluidity and low compression crushing properties. First, the purchased river sand was dried, and impurities and gravel particles were manually removed. Screening produced coarse sand with an average particle size of 1~0.5 mm and fine sand with an average particle size of 0.25~0.125 mm.

Soils with low fluidity and high compression crushing properties. Following the drying of the soil, impurities and gravel particles were removed manually. The more uniform 8 mm and 4 mm single soil particles were obtained via screening.

8 mm ceramsite with superior fluidity and excellent compression breakage. The ceramsite is made of clay after high-temperature roasting and expansion. Its interior is a honeycomb structure, which has the characteristics of low strength, high porosity, and low cost. Ceramsites were purchased in Yichang City, Hubei Province. Before use, the low-strength lightweight ceramsites were dried in the sun, and the broken and incomplete particles were manually removed, and then more uniform 8 mm single-grain ceramsites were obtained after screening.

The selected granular filling materials are shown in Figure 3, and their physical parameters are listed in Table 1. The particle size distribution curve of the granular material is shown in Figure 4.

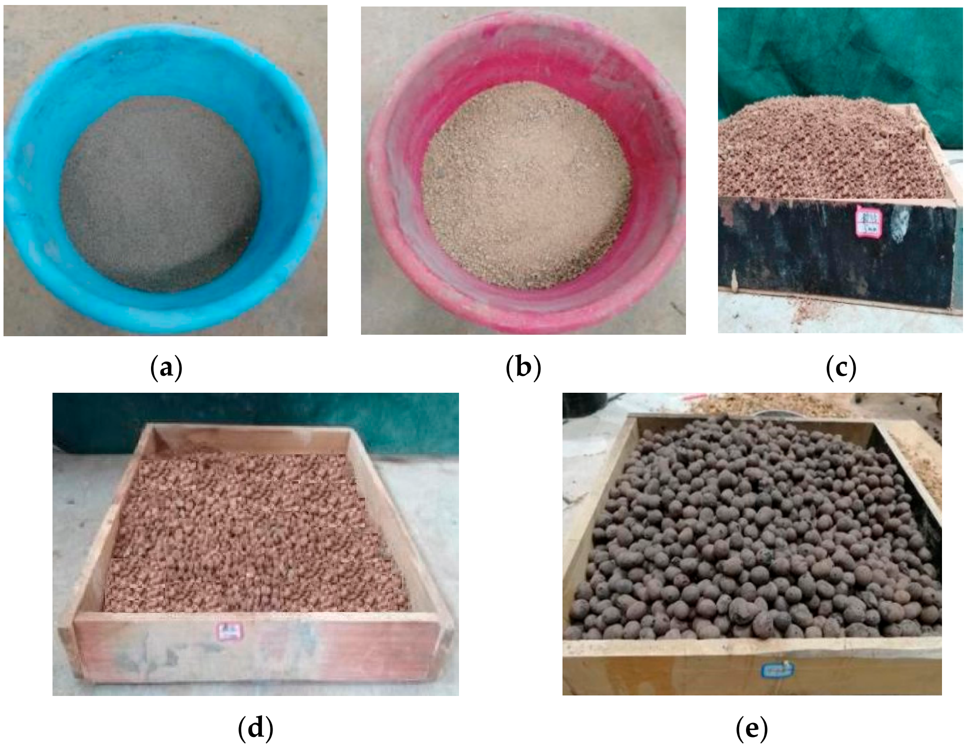

Figure 3. Granular filling materials. (**a**) Fine sand with particle size < 0.25 mm. (**b**) Coarse sand with particle size > 0.5 mm. (**c**) Soil with a 4 mm particle size. (**d**) Soil with an 8 mm particle size. (**e**) Ceramsite with an 8 mm particle size.

Table 1. Physical parameters of the filling materials.

Material Categories	Natural Void Ratio	Natural Moisture Content (%)	Density (g/cm^3)	Bulk Density (g/cm^3)	Permeability Coefficient (m/d)
Fine sand	0.071	10	2.60	1.65	1.20
Coarse sand	0.143	15	2.55	1.60	25.50
4 mm soil	0.518	18	2.55	1.70	0.30
8 mm soil	0.908	22	2.50	1.68	0.45
Ceramsite	0.475	10	1.40	0.60	6.60

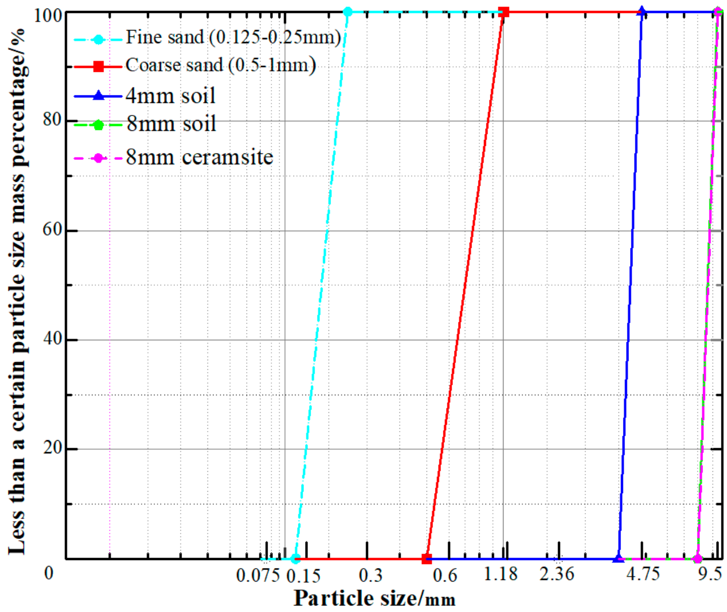

Figure 4. Particle size distribution curve of granular materials.

3.2. Test Method

A confined compression test was conducted using the developed simulated loading test device. The device was filled with coarse sand, fine sand, 4 mm soil, 8 mm soil, and 8 mm ceramsite to the same height, i.e., h = 150 mm. Electrohydraulic jacks were employed to apply different load grades to simulate the local deformation of soft-rock tunnels with high ground stress on five kinds of compressible granular material-filled lining support structures. The settlement, reaction force, and stress response of sand, soil, and ceramsite under different levels of concentrated force load were quantitatively studied. Thus, the law of deformation settlement and the supporting effect of the five fillers were quantitatively investigated.

Loading test device: A Q235B steel plate with a thickness of 12 mm was used for welding the pressure loading box without a lid for increased strength. Its size was 25 mm × 25 mm × 25 mm. The device simulated the unidirectional deformation of the compressible granular filling material lining. The top was loaded with an electrohydraulic jack in 2 kN steps, as shown in Figure 5.

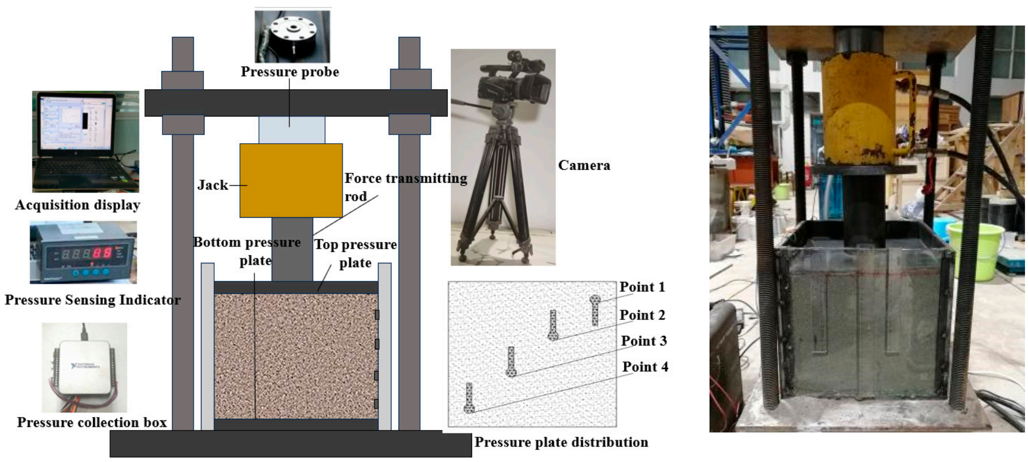

(**a**) Schematic diagram of confined compression test system (**b**) Physical diagram of device

Figure 5. Experimental system.

Data collection: The experimental data collection setup is shown in Figure 4. The pressure and sedimentation values of the filling material at each loading level were recorded. When the settlement of two successive loading levels was less than 1 mm, loading was terminated.

High-definition camera: The whole model box process was tracked and photographed to capture the evolution of the particle sample during the whole test.

Pressure sensor calibration: a. The pressure sensor connection, signal wiring, and power supply were checked to ensure proper operation. The sensor's instructions were followed for zero adjustment. b. The calibrator was connected to the pressure sensor and a series of known pressures were applied through the calibration pump. c. The pressure value displayed by the calibrator corresponding to the pressure sensor output was recorded. The calibration had to cover the desired measurement range and be multi-point at different pressures.

Control data results accurately: a. Data processing and comparisons based on the data recorded during the calibration process were performed. Pressure sensor measurement error was calculated. Calibration results were compared with the standard error requirements to assess whether the accuracy of the pressure sensor met the requirements. b. If there was a large deviation in the calibration results, appropriate adjustments and corrections were made according to the calibration method provided by the manufacturer until the accuracy requirements were met.

4. Study of the Mechanical Properties of Different Filling Materials

4.1. Regularity Analysis of the Strain of Granular Filling Materials

Compressive strain [38] reflects the degree of deformation of the filling material under confined conditions under load. The cross-sectional area of the filling material is the same during the deformation process. Compressive strain is related to pressure, which reflects the filling material's compressibility. The law of compressive strain of granular filling affects the development of plastic zone of surrounding rock, the force on the lining, and the engineering effect of granular filling lining support stage II. Equation (3) shows the compressive strain formula.

$$\varepsilon_s = \frac{\sum \Delta h_i}{h_0} \times 100\% \tag{3}$$

where ε_s represents the compressive strain (expressed as a percentage), $\sum \Delta h_i$ represents the total deformation of the specimen after compression under a certain pressure, and h_0 indicates the initial height of the sample.

In the experiment, after four compressible granular fillings of fine sand, coarse sand, 4 mm soil, and 8 mm soil had been loaded to 60 kN, they no longer deformed. They entered the deformation stop stage. After the ceramsite was loaded to 115 kN, the deformation stopped and the ceramsite entered the deformation stop stage.

4.1.1. Pressure–Strain Relationship Curves of Granular Materials

As can be seen in Figure 6, (1) the pressure–strain curve is generally convex, that is, the compressive strain of each sample increased nonlinearly with the increase of vertical pressure, and the rate of increase of compressive strain gradually slowed down with the continuous increase of pressure, and the sample became more difficult to handle. (2) As compared with each sample, the maximum compression strain was for 8 mm soil, the minimum compression rate was for fine sand, and the compression rates of 4 mm soil, coarse sand and ceramsite were between 8 mm soil and fine sand.

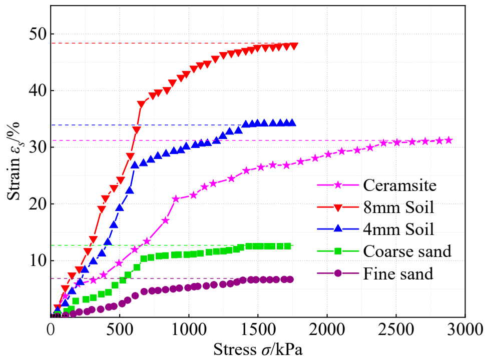

Figure 6. Particle stress–strain curve.

4.1.2. Analysis of the Compressive Strain Mechanism

(1) Compressive strain of 8 mm and 4 mm soil particles

Soil particles have higher compressive strain, mainly due to the larger particle size, the greater inter-particle voids and pores of the particles, and weaker pressure-resistant properties. In the early stage of loading, the compressive strain rate was larger due to large inter-particle voids, a large particle–void ratio (as shown in Figure 7), and particle dislocation (as shown in Figure 8). In the later stages, the inter-particle voids were filled, and crushing and recombination were gradually consolidated, and the strain rate was reduced until the strain limit was reached.

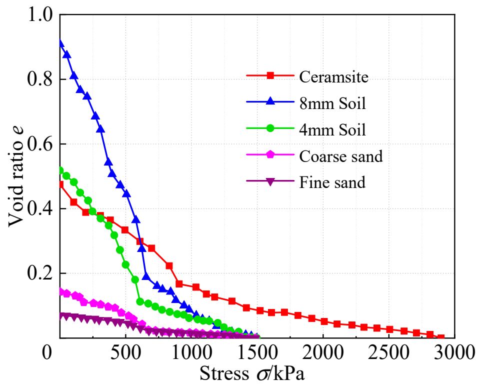

Figure 7. Particle stress–void ratio curve.

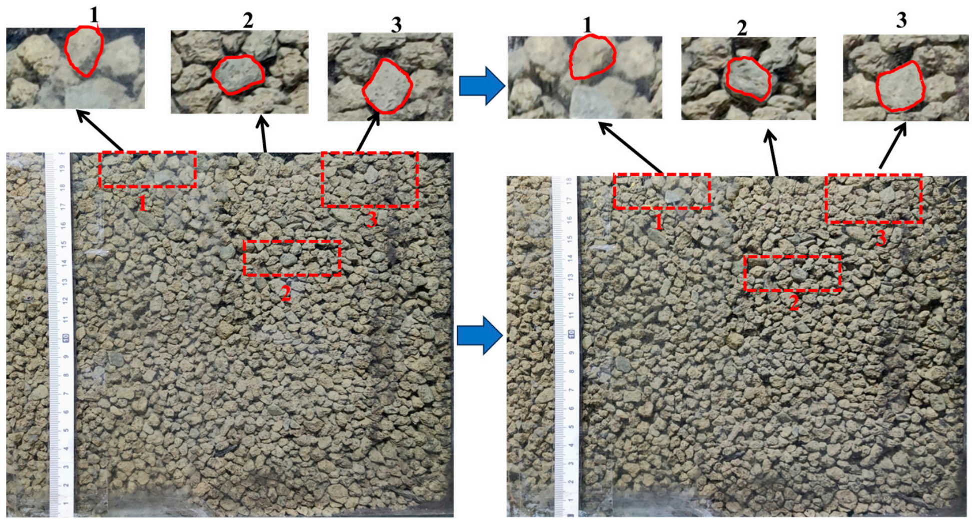

(**a**) 8 mm soil particles

Figure 8. *Cont.*

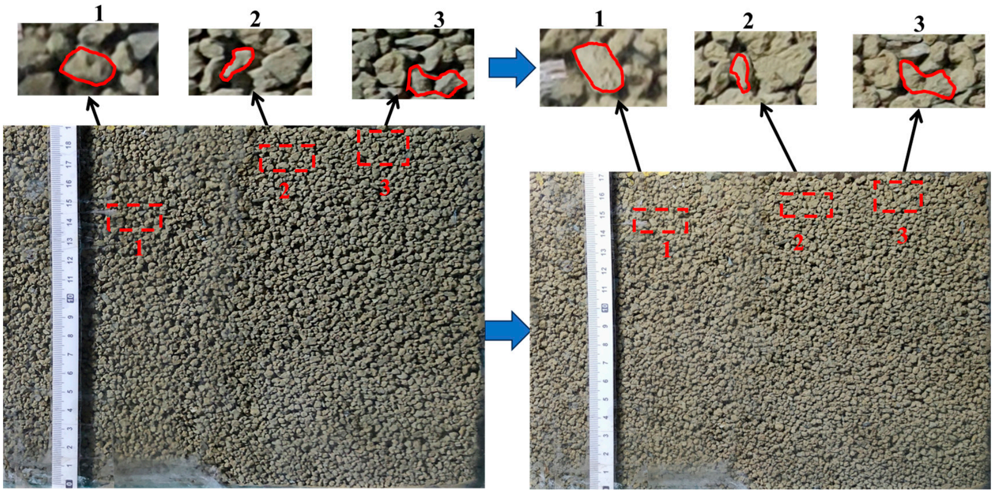

(**b**) 4 mm soil particles

Figure 8. Particle dislocation before and after compression of soil particles.

As can be seen in Figure 9, the crushing effect of the upper layer was more significant than that of the lower layer when soil particles were broken. The reason is that the upper layers absorbed deformation energy and destroyed it during compression, and passed it down layer by layer. The particle size, inter-particle voids and particle pores of 8 mm soil are larger than those of 4 mm soil, so its compressive strain was also larger.

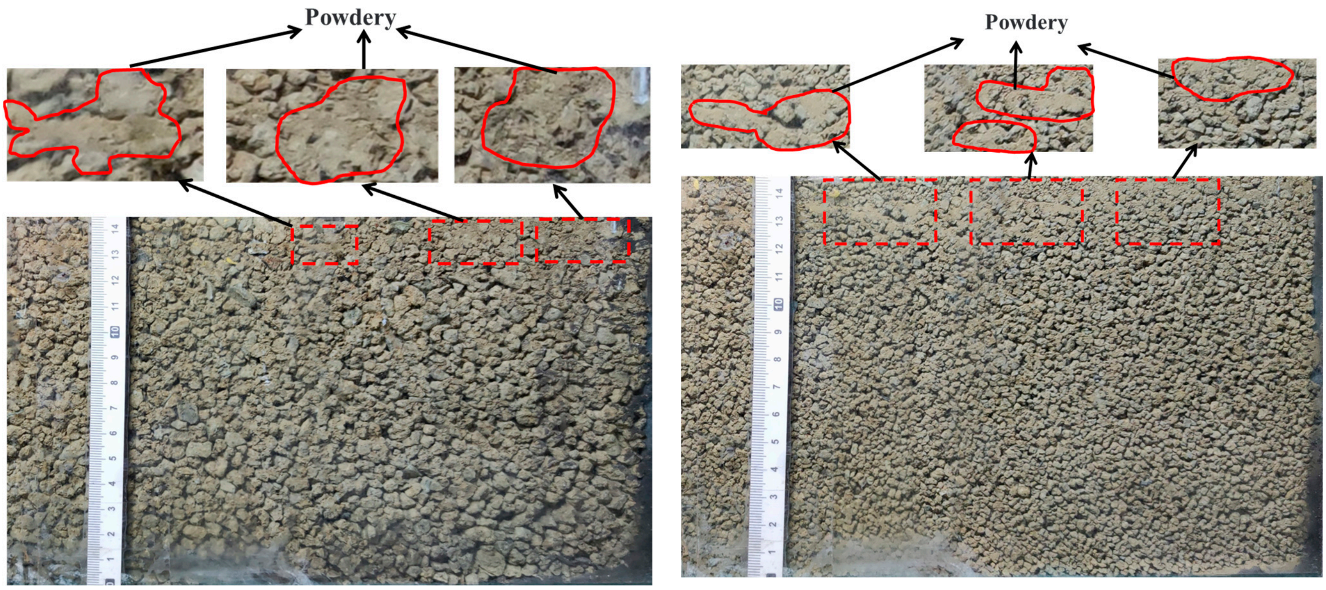

(**a**) 8 mm soil particles (**b**) 4 mm soil particles

Figure 9. Soil particle breakage in the compression process.

(2) Compressive strain of ceramsite particles

Ceramsite particles have high porosity due to their internal honeycomb structure, which leads to greater compressive strain (see Figure 6). During the early stages of the compression process, due to the mutual extrusion of loose ceramsite under load, interparticle voids and particle pores decreased. This resulted in a higher strain rate. In the later stages, due to the continuous extrusion of particles, the particles were broken, flaky particles filled the voids, and the compressive strain was reduced.

(3) Compressive strain of coarse sand and fine sand

As compared with other particles, sand has a higher density, smaller porosity, and a lower coefficient of crushing, resulting in a smaller compressive strain (as shown in

Figure 6). Sand compression is primarily due to the compression of pores between the particles, and the particles themselves do not deform due to compression. The porosity of coarse sand is significantly higher than that of fine sand, so the compressive strain of coarse sand is greater than that of fine sand.

In summary, it can be seen that the compressive strain of 8 mm soil was the largest, and its ability to yield to deformation as a granular material-filled lining was the best, which can ensure that the surrounding rock allows its plastic zone to develop under a certain supporting force, release the surrounding rock pressure to the greatest extent, and reduce the force on the lining.

4.2. Analysis of the Load Reduction Law of Compressible Granular Filling Materials

The load reduction value and load reduction rate of different compressive strains were generated using Equations (4) and (5). In addition, the load reduction rule for filling was analyzed. Before the analysis, we considered friction between the particles and the side walls. Because the side wall was smooth, the side wall was coated with a layer of silicone oil to reduce its friction; in addition, according to the relevant literature [39], the friction coefficient between the particle and the side wall ranges from 0.17 to 0.20, and the calculated friction force based on the measured side wall pressure is much smaller than the pressure difference between the top and bottom of the particle, so the influence of friction was ignored when studying the load shedding rule. Figure 10 shows the filler force diagram.

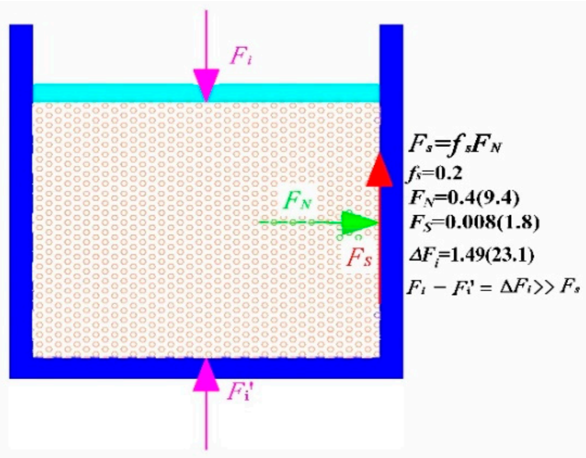

Figure 10. Schematic diagram of the force on the filling.

$$\Delta F_i = F_i - F_i' \tag{4}$$

$$\eta_i = \frac{\Delta F_i}{F_i} = \frac{F_i - F_i'}{F_i} \tag{5}$$

In the formula, ΔF_i is the load reduction value of the class i load, F_i is the class i load value, F_i' is the pressure value at the bottom of the confining box of the class i load, F_i and F_i' are shown in Figure 10, and η_i is the class i load reduction rate. η_i denotes the reduction capacity of the granular filler to the applied load at each level of load applied. The larger the value, the better the load reduction capacity, and vice versa, the worse the effect.

In order to further study the reduction effect of granular materials on the applied load, according to the reduction load rate and compressive strain of granular fillings, the compressive strain–load shedding rate curve was drawn, as shown in Figure 11 below.

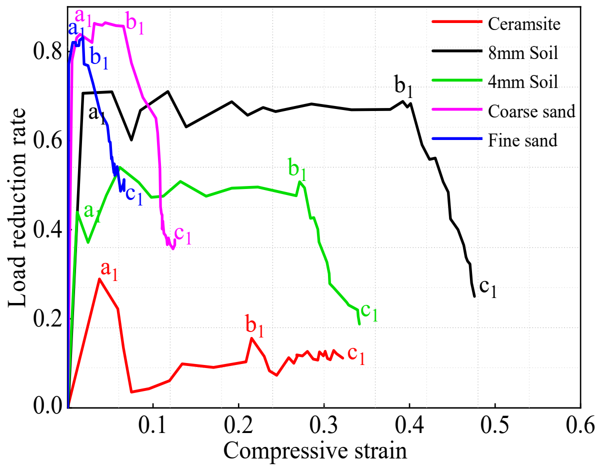

Figure 11. Compressive strain–load shedding rate law.

4.2.1. Stage Division of Granular Filling Load Shedding Rate

As can be seen from Figure 11, according to the variation characteristics of the compressive strain–load shedding rate curve of the particle-filled material, load shedding was divided into three stages: (1) Rapidly increasing section of the load shedding rate (oa); i.e., η_i increased linearly and rapidly; (2) Steady-state peak load rate reduction section (ab); i.e., after the granular filling materials reached the peak load reduction rate η_{max}, they maintained η_{max}, a minute float; and (3) Drop stage of the load reduction rate η_i (bc); i.e., the load reduction rate η_i began to fall after it reached η_{max}, and η_{max} is defined as the start value of the load reduction rate drop.

4.2.2. Analysis of the Load Reduction Rate at Each Stage

(1) Load reduction rate rapid improvement section (oa)

Before compressive strain = 0.03, all filling materials reached a peak load reduction rate. At this stage, load reduction was the fastest. The order of load reduction rate of different granular fillings was ceramsite < 4 mm soil < 8 mm soil < coarse sand < fine sand.

Accordingly, particle dislocation occurred in each particle-filled material at this stage. The filling material force skeleton was not completely formed. The upper load was dissipated due to particle dislocation, and the load reduction rate increased rapidly. Fine sand reached peak load reduction rate most quickly due to its small particle size and easy dislocation.

(2) Steady-state peak load rate reduction section (ab)

After the particle filling load reduction rate reached its peak value, when the compressive strain increased greatly, the load reduction rate remained stable. This means it had the maximum load reduction effect in steady state. In order to facilitate the analysis of the maximum reduction effect of steady state, the evaluation index S was introduced.

S is the area enclosed by the steady-state peak load reduction rate and the *X*-axis compressive strain, which is used to represent the ability of the particle filling to retain the energy generated by the compressive strain to the greatest extent, that is, the ability of the particle to absorb the maximum elastic potential energy. The larger the *S*, the better the particle's ability to absorb maximum elastic potential energy, and vice versa. Formula (6) shows the evaluation index *S*.

$$\begin{aligned} S &= \int_a^b (\varepsilon_b - \varepsilon_a)\eta_{\max} dx = \int_a^b \Delta\varepsilon_{ba} \left(\frac{\Delta F_i}{F_i}\right)_{\max} dx \\ &= \int_a^b \frac{\Delta h_{ba}}{h_0} \frac{\Delta F_i}{F_i} dx = \int_a^b \left(\frac{\Delta E}{E}\right)_{\max} dx \end{aligned} \quad (6)$$

In the formula, ε_a and ε_b represent the compressive strain at points a and b, $\Delta\varepsilon_{ba}$ represents the difference between the compressive strain at points a and b. $\eta_{\max}$ represents the peak value (maximum value) of the reduction load rate; ΔE represents the elastic potential energy absorbed by the particles, and E represents the total elastic potential energy of the granular materials.

Table 2 shows that 8 mm soil had the strongest ability to absorb elastic potential energy. The reason is that 8 mm soil particles are larger and the internal pores are more numerous. At this stage, the force skeleton is basically formed. The load reduction rate remains unchanged after reaching the peak, so the ability to absorb elastic potential energy is stronger. The order of the granular filling's ability to retain elastic potential energy from strong to weak was 8 mm soil > 4 mm soil > coarse sand > fine sand > ceramsite.

Table 2. Statistical table of the steady-state peak section of the reduced loading rate.

Parameter / Filling Material	η_{max}	ε_a	ε_b	S
8 mm soil	0.7	0.021	0.397	0.2632
4 mm soil	0.51	0.061	0.277	0.11016
coarse sand	0.85	0.031	0.065	0.0289
fine sand	0.82	0.006	0.013	0.00574
ceramsite		0.037	0.037	0

(3) Drop section of the load reduction rate (bc)

At this stage, the load reduction rate of the particles decreases, i.e., the ability of the particles to reduce the load diminishes until the load reduction rate is minimized. At this time, the compressive strain of the particles reaches maximum, the porosity is the lowest, and the particles are almost incompressible.

In summary, fine sand had the fastest speed to reach the peak load reduction rate. In the early stages of loading, fine sand had a better load reduction effect under the small compressive strain. The 8 mm soil had a strong ability to absorb elastic potential energy. When the compressive strain changed greatly, 8 mm soil had a significant load reduction effect, and the overall load reduction effect was the most efficient.

4.3. Analysis of the Change Rule of Horizontal Stress in Compressible Granular Filling Material

The filling particles were extruded by the vertical load and expanded downward to produce horizontal stress. To study the variation rule of the horizontal force along the depth of the filling material, four pressure sensors were uniformly set along the depth direction of the loading box. The pressures were named F_1, F_2, F_3, and F_4 from top to bottom. The change patterns of the horizontal force of soil, sand, and ceramsite were analyzed.

4.3.1. Evolution Model of Soil Horizontal Force

(1) Evolution law of horizontal force

When the filling material was soil, the variation rule of the horizontal force is shown in Figure 12.

As shown in Figure 12, at the beginning of the test, with increasing load, the pressures at the four points on the sidewall gradually increased. The pressures at the four points of 8 mm soil and 4 mm soil were $F_1 < F_2 < F_3 < F_4$. As the pressures continued to increase, the speeds of the lateral wall pressure increase were at $0.037 < e < 0.160$ for 8 mm soil and $0.058 < e < 0.112$ for 4 mm soil and began to change. At first, F_3 exceeded F_4, and then F_2 and F_1 exceeded F_4 when $e < 0.037$ for 8 mm soil and $e < 0.058$ for 4 mm soil. The pressures at the four points were $F_1 > F_2 > F_3 > F_4$.

The author's analyses show that a soil arch is produced by the relatively uneven settlement of soil particles during the shear, compression, and compaction process under overburden load. A soil arch can only form when two conditions are met: an arch foot that supports it, and uneven soil displacement. The evolution of a soil arch is shown in Figure 13.

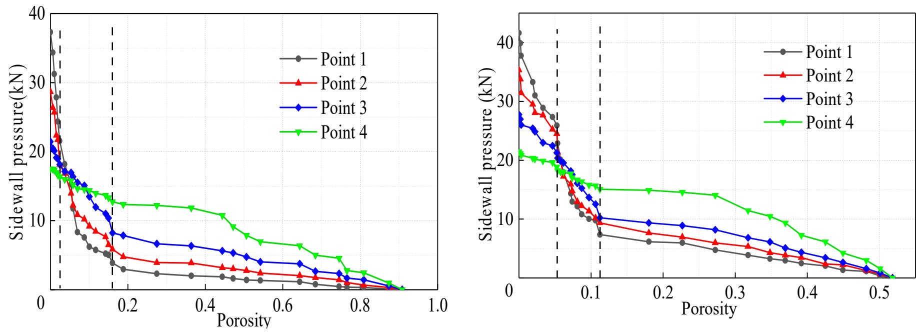

(**a**) 8 mm soil (**b**) 4 mm soil

Figure 12. Soil porosity–sidewall pressure.

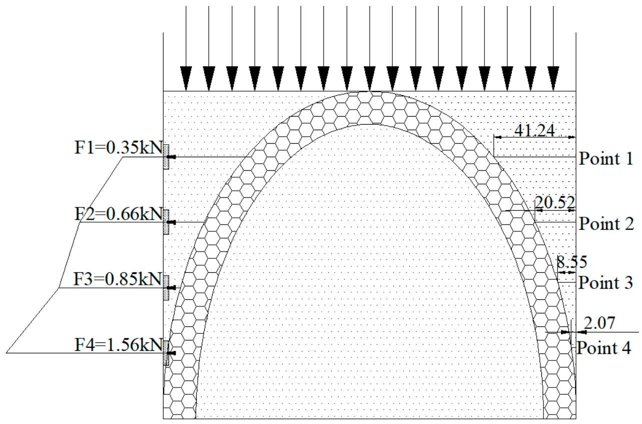

(**a**) Initial soil arch forming stage

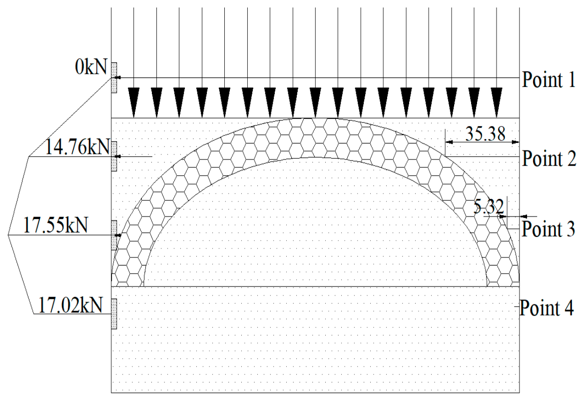

(**b**) Arch foot upward movement stage

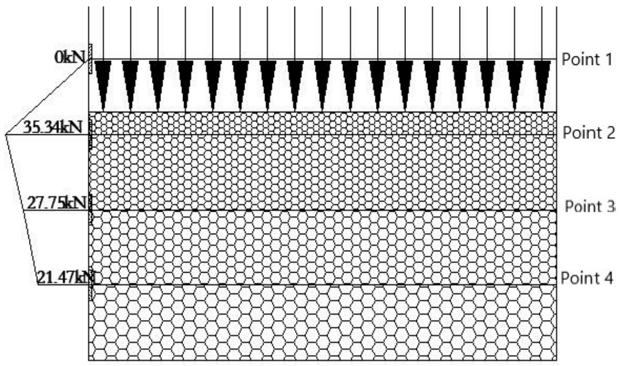

(**c**) Soil arch disappearance stage

Figure 13. Schematic diagram of soil arch change.

The soil-arch effect changes the direction of pressure transfer, resulting in the arch foot taking on the upper load. The outer side of the soil arch is the stress shield zone. The closer it is to the top, the larger the shield zone range, and the smaller the horizontal force *F*. With increasing load, the particles at the arch foot are compacted, the arch foot moves upwards, and the maximum horizontal force becomes F_4, F_3, and F_2.

Based on the above analysis, a visualization soil particle confined compression test was carried out, as shown in Figure 14. The graduated scales were arranged in the left, middle and right positions on the visualization surface of the confined pressure box. One layer of pigment was laid every 50 mm in the confined pressure box. The compression displacement of each pigment layer was observed during compression. According to the displacement of the soil arch, the evolution process of soil arch was observed, and then the soil compression and movement law at each location were studied more intuitively.

Combined with Figure 12 and the compression displacements of each soil layer during compression, schematic diagrams of the evolution law of the soil arch were drawn, as shown in Figure 15.

Figure 14. Initial diagram of the visual compression test.

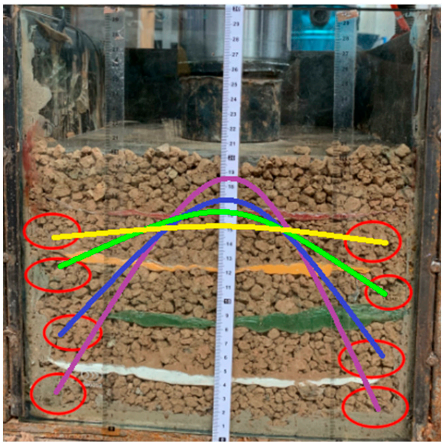

Figure 15. Distribution diagram of morphological characteristics of the soil arch evolution process.

The settlement patterns of different stratified soils at five points are shown in Figure 16.

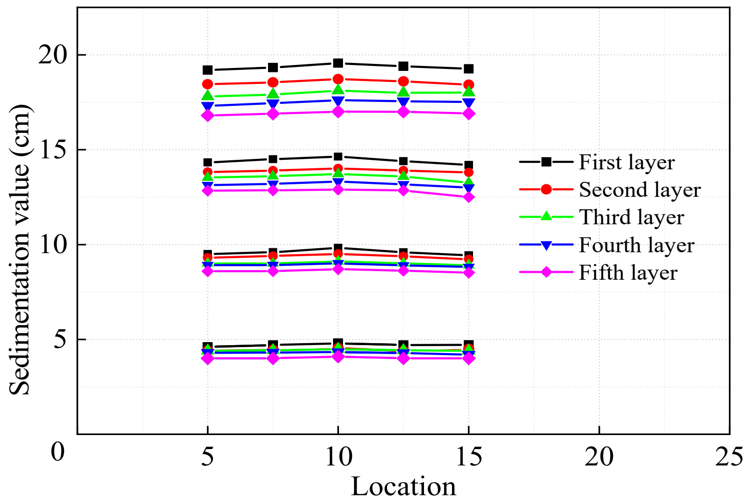

Figure 16. Settlement law of soil in different layers at different points.

As shown in Figure 16, except for the bottom layer, the settlement amount in the middle of each layer was less than that at both ends. With increasing load, particles at the position of the arch foot were compacted and crushed (as shown in Figure 14), and the arch foot gradually moved upwards. Finally, the settlement value at each point in the same layer approached a horizontal line, confirming the correctness of the soil arch effect analysis.

(2) Soil arch horizontal force transfer law

Assuming that the load reduction rate decreases uniformly along the soil thickness, according to Formula (7), the load reduction coefficient per unit of soil thickness λ was calculated. According to the principle of three-hinged arch structures, the arch axis form is parabolic [40–42]. The distance x_i between the soil arch and the sidewall was calculated using a parabolic geometric relationship. The horizontal force of the soil arch at different heights was deduced by combining x_i and sidewall pressure F_i through Formula (8). The variation rule of the horizontal force at different heights of the soil arch under various loads is shown in Figure 17:

$$\lambda = \frac{\Delta F_i}{h_i} = \frac{F_i - F_{i-1}}{h_i} \tag{7}$$

$$F_i{}' = F_i + \lambda x_i \tag{8}$$

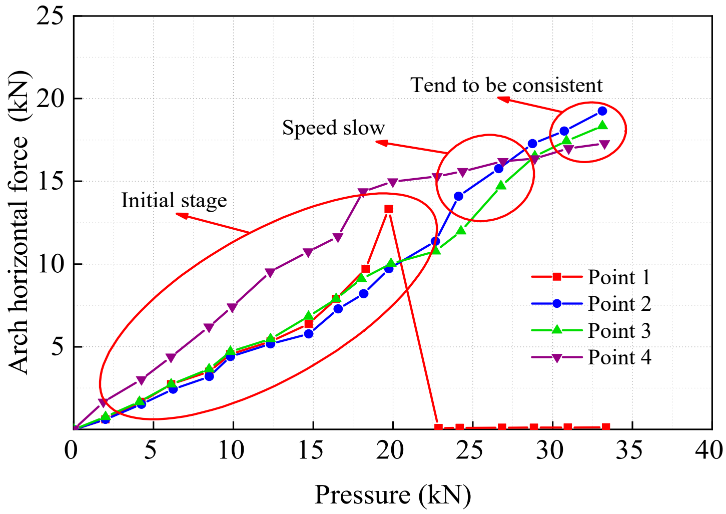

Figure 17. Variation of horizontal force at different heights of soil arch under different loadings.

As seen in Figure 17, in the initial stage of the soil arch, the horizontal component F_4 was significantly larger than that of other positions. The pressure at other positions of the soil arch was the same, proving that most of the load was shared by the arch feet. With increasing pressure, horizontal component F_4 slowed down. The arch foot gradually moved upwards until the final soil arch disappeared, and the horizontal force at each point tended to be the same.

4.3.2. Evolution Model of the Horizontal Force of Ceramsite

The variation law of the horizontal force of ceramsite with porosity is shown in Figure 18.

Figure 18 shows that ceramsite's horizontal force decreased with increasing depth throughout the experiment, namely, $F_1 > F_2 > F_3 > F_4$. The suggested reason is that ceramsite roundness is good, the settlement is homogenized in the compression process, the ceramsite at the top is crowded and broken first, and the horizontal force is the largest. The closer to the bottom of the loading box, the lower the extrusion degree of particles and the lower the horizontal force.

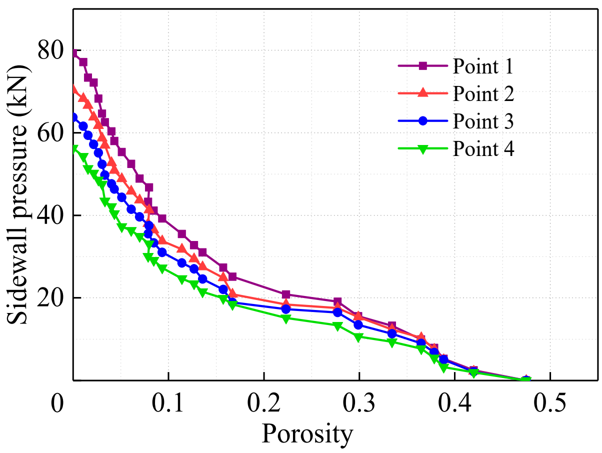

Figure 18. Porosity–lateral pressure diagram for ceramsite.

4.3.3. Evolution Model of Sand Horizontal Force

The variation law of the horizontal force of sand with porosity is shown in Figure 19.

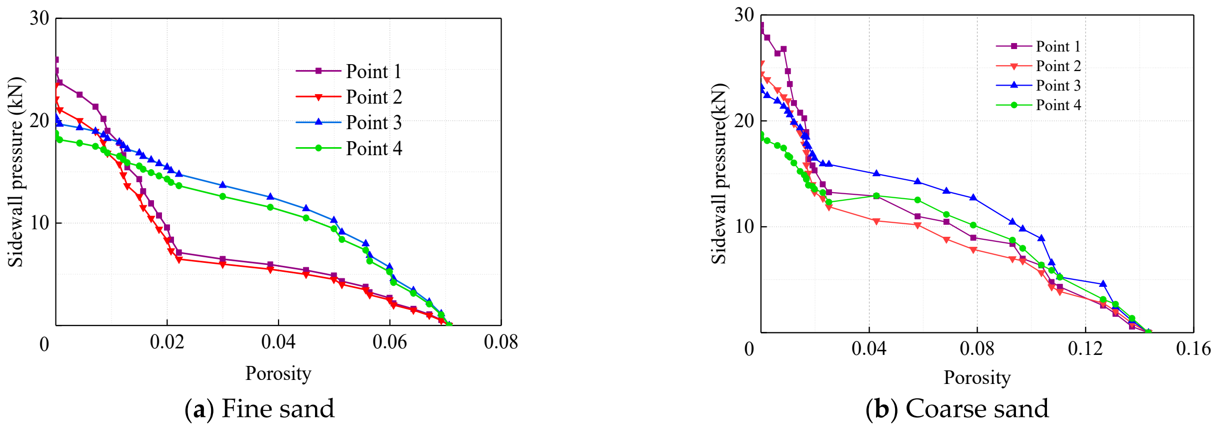

Figure 19. Porosity–lateral pressure diagram for sand.

As shown in Figure 19, when the filling was sand, at the initial stage of compression, the pressure at point 3 was the maximum, the pressure at point 2 was the minimum, and the pressure at points 1 and 4 was between that at points 2 and 3. When the filling material was sand, the horizontal force evolution model was between the soil arch model and the ceramsite layering pattern.

4.3.4. Comparison of Horizontal Force Evolution Models of Different Compressible Granular Filling Materials

Figure 20 shows horizontal force evolution models of different compressible granular fillings at points 1, 2, 3, and 4.

Figure 20 shows that the horizontal forces of the five compressible granular fillings of 8 mm soil, 4 mm soil, ceramsite, fine sand, and coarse sand increased with a decrease in porosity from point 1 to point 4. Ceramsite's horizontal force increased more readily, and was strongest when destroyed by compaction. The horizontal force of fine sand was the smallest among the five compressible granular fillings. The horizontal forces of soil and coarse sand were between those of ceramsite and fine sand.

Due to the excellent roundness of the ceramsite, in the process of gradual loading, the ceramsite moved around. However, the ceramsite could not move along the sidewalls because of lateral constraints. This resulted in enormous pressure on the sidewall and a remarkably rapid growth rate. Because fine sand has smaller porosity than other compressible granular fillings, the density was higher. The lateral wall pressure and growth rate for fine sand were smaller than those for the other four compressible granular fillings in the loading process.

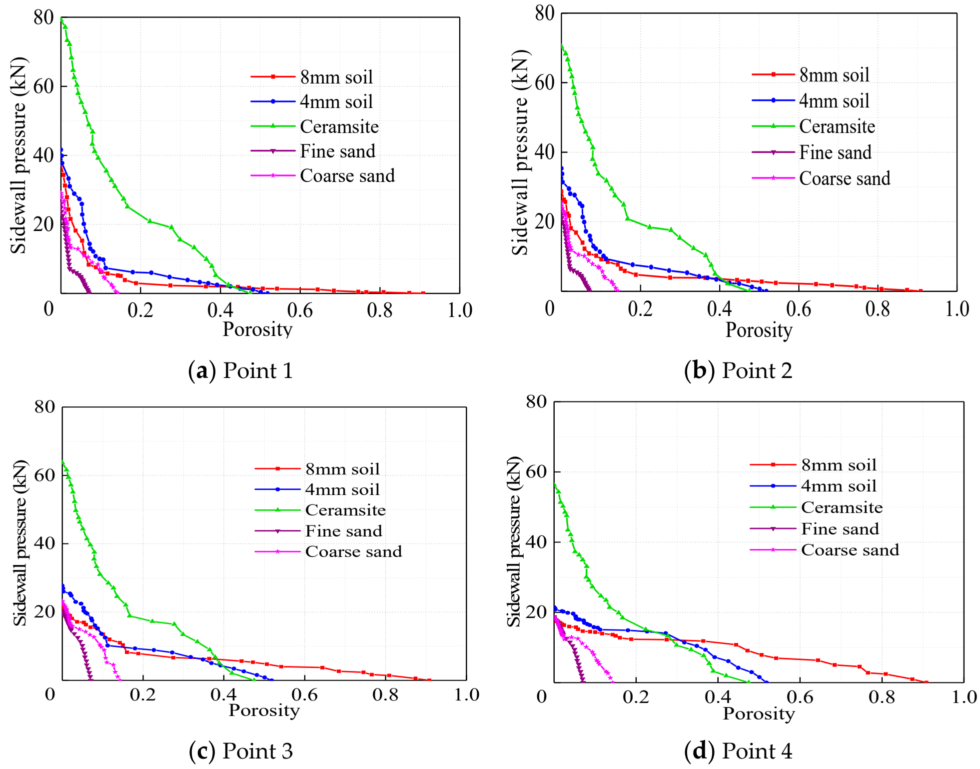

Figure 20. Comparison of the horizontal forces of different compressible granular fillings.

5. Study of the Yielding-Pressure and Relief-Pressure Mechanism of Compressible Granular Filling Lining

5.1. Analysis of the Supporting Effect of Compressible Granular Filling

5.1.1. Test Introduction

The author used a self-developed supported beam device with a pressure relief valve to simulate the straight-line section of the tunnel. The pressure relief mechanism of compressible granular filling lining was studied through the discharge and load reduction of compressible granular filling. The overall test device and schematic diagram are shown in Figure 21.

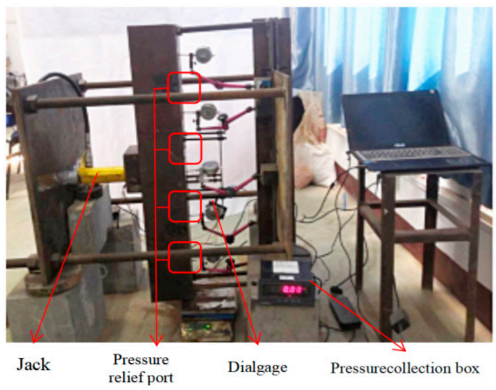

Figure 21. The overall test device of the supported beam.

(1) Test device. The supported beam was made of Q235 steel channel of 158 mm × 158 mm × 8 mm with a length of 1200 mm. Both ends of the steel channel were welded to plates of the same thickness of 158 mm × 158 mm. The steel channel's elastic modulus was 200 GPa.

(2) Monitoring point arrangement. Five pressure monitoring points were arranged on the inner surface of the steel channel bottom of the supported beam. These points measured the pressure value after load reduction through a compressible granular filling buffer layer. The strain monitoring points corresponded to the pressure monitoring points on the outer side of the bottom of the steel channel. This was to monitor the strain value on each point during the loading process. The arrangement of pressure and strain monitoring points is shown in Figure 22.

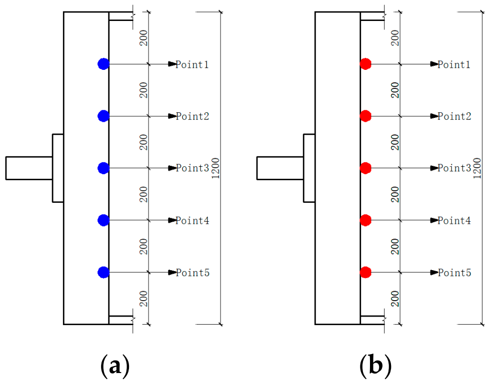

Figure 22. Layout of the stress and strain monitoring points. (**a**) Pressure monitoring points arrangement. (**b**) Strain monitoring points arrangement.

(3) Pressure relief port setting. Four pressure relief ports were placed at the bottom of the steel channel supported beam. When the load at the bottom of the supported beam reached the set threshold, the pressure relief port automatically opened to discharge sand. When the pressure decreased, the pressure relief port would be closed again.

(4) Installation of compressible granular filling material. According to the previous confined compression test, fine sand was selected as the research object. This selection considered the compressibility, compressible granularity, and leakage of the granular filling. First, the device was rotated 90° anticlockwise, fine sand was added and paved in the steel channel in advance, a 150 mm × 1200 mm steel plate of 25 mm thickness was taken as the pressure plate at the opening end of the steel channel and fixed to the steel channel, the device was rotated and put in place, and the hydraulic jack was installed.

(5) Test conditions. After loading the test device to 60 kN, the compressive strain of fine sand tended to be stable, and the unloading stage began. Three working conditions were adopted in this test: the first working condition was to load the steel channel without the sand filling; the second working condition was to conduct a loading test on the steel channel with the sand filling but without sand discharging; and the third working condition was to carry out a loading test on the steel channel with the sand filling and sand discharging. Figure 23 shows the different working conditions.

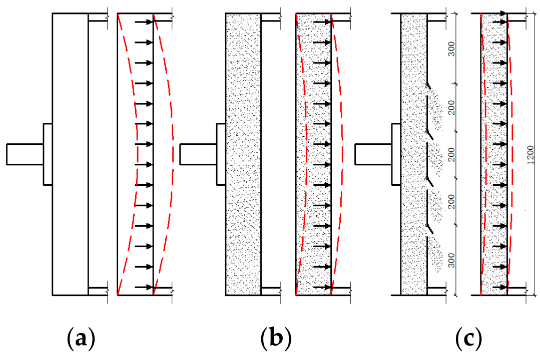

Figure 23. Forces diagram of the supported beam under different working conditions. (**a**) Structure with no filling-sand. (**b**) Structure with filling-sand before sand discharge. (**c**) Structure with filling-sand after sand discharge.

5.1.2. Comparative Analysis of Deflection

To compare and analyze the deflection changes of the monitoring points of supported beams without fine sand, supported beams with the fine sand filling before pressure relief, and supported beams with the fine sand filling after pressure relief, the deflection values of the monitoring points recorded in the test are plotted in Figure 24.

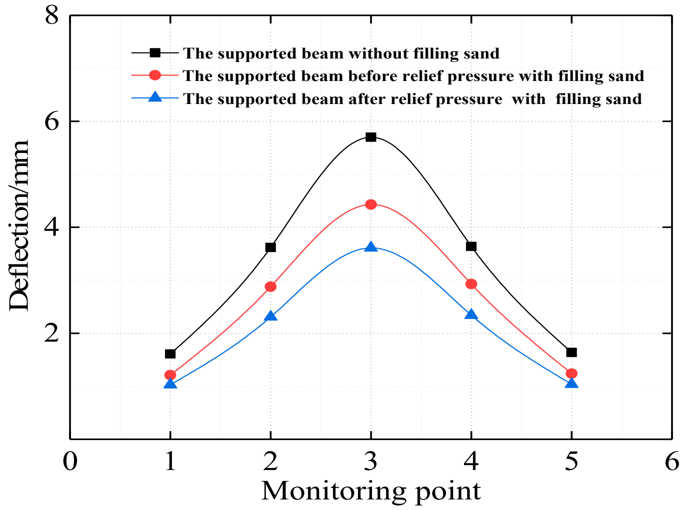

Figure 24. Comparison of deflection changes.

Figure 24 shows that the deflection of the supported beam without compressible granular filling sand was the largest, the deflection before relief pressure of the supported beam with filling sand was second, and the deflection after relief pressure of the supported beam with filling sand was the smallest. The maximum deflection reduction rate before relief pressure of the supported beam with filling sand and without compressible granular filling sand was 22.8%, and the maximum deflection reduction rate after pressure relief and before pressure relief of the supported beam with filling sand was 20%. The maximum deflection reduction rate after pressure relief and without filling sand was 36.7%.

5.1.3. Comparative Pressure Analysis

The optimum bottom pressure of the supported beam without the sand filling was 56.34 kN. The maximum bottom pressure of the supported beam with the sand filling and before relief pressure was 29.41 kN. The maximum bottom pressure of the supported beam with the sand filling and after relief pressure was 12.34 kN. The pressure reduction rate of supported beams with the sand filling and before pressure relief and without sand filling was 47.8%. The pressure reduction rate of the sand filling before pressure relief and after pressure relief was 58%, and the pressure reduction rate of the sand filling after pressure relief and without sand filling was 78%.

By comparing the deflection and pressure of the supported beam without the sand filling and the supported beam with the sand filling, it can be seen that the deflection and pressure of the supported beam with the sand filling were significantly lower than those of the supported beam without the sand filling. The reason is that sand mobility homogenizes the supporting force. Sand absorbs pressure generated by the deformation of the surrounding rock. This reduces the deflection and pressure on the second lining, which provides a better yielding-pressure effect. By comparing the deflection and pressure of the supported beam with sand applied before pressure relief and after pressure relief, it can be seen that the deflection and pressure of the supported beam after pressure relief were significantly reduced because the discharge of compressible granular filling sand released part of the pressure applied by the surrounding rock, which further decreases the deflection and pressure on the secondary lining. The pressure which the compressible granular filling sand was able to absorb and release from the surrounding rock in the middle of the supported beam was higher than that at both ends. It tended to decrease gradually from the peak in the middle towards both ends.

5.2. Energy Transformation of the Granular Material Filling Lining

After tunnel excavation, stress is redistributed. Relevant scholars [43] have studied energy transformation in tunnel excavation. Equations (9) and (10) describe the law of energy transformation in tunnel excavation:

$$W_c + U_m = U_c + W_n + W_f + W_r \tag{9}$$

$$U_c + W_n + W_f + W_r \approx constant \tag{10}$$

where W_c is the work done by the internal stress of the rock mass during excavation; U_m is the strain energy released by the excavation of the rock mass; U_c is the elastic energy reaccumulated by the rock mass after tunnel excavation; W_n is a part of the inelastic energy of the loss of viscosity, plasticity and brittle fracture of the surrounding rock; W_f is the energy absorbed by the lining support structure; and W_r is the elastic energy lost during tunnel excavation.

According to Equation (9), overall tunnel safety can be improved by improving W_f. The granular material filling lining is designed based on this idea, as shown in Equations (11) and (12).

$$W_f = W_{fe} + W_{fc} \tag{11}$$

$$W'_f = W_{fe} + W'_{fe} + W'_{fc} + W_{unload} \tag{12}$$

Equation (11) is the energy W_f absorbed by the traditional supporting structure. The energy absorbed by the lining structure comprises elastic energy W_{fe} and plastic energy W_{fc} (as shown in Figure 25a). Equation (13) represents the energy W'_f absorbed by the support structure of the granular material filling the lining. This consists of the elastic energy W_{fe} of the lining structure, the elastic energy W'_{fe} of the filling material, the plastic energy W'_{fc} of the filling material, and the energy released W_{unload} by the granular material (as shown in Figure 25b). The lining structure does not produce plastic strain energy W_{fc}.

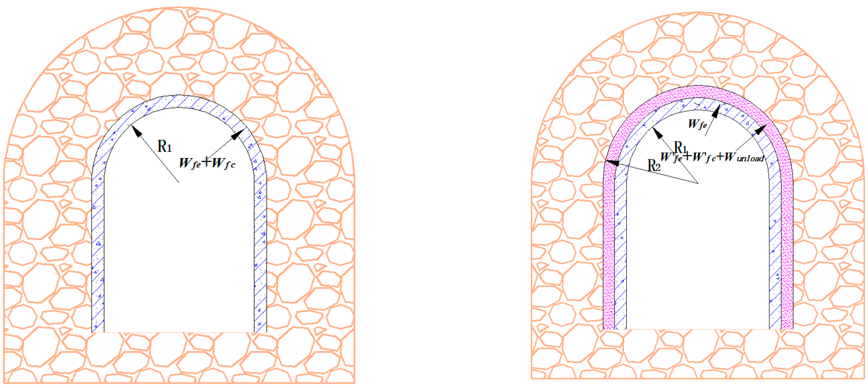

(**a**) Traditional support structure (**b**) Compressible granular filling lining support structure

Figure 25. Comparison of the energy absorption of the supporting structure.

5.3. Analysis of the Energy Consumption of the Compressible Granular Filling Material

The energy consumed by the granular material that fills the lining is partly the energy $W_{compress}$ absorbed by compressible granular filling compression and crushing. It is also partly the energy W_{unload} released by the compressible granular filling.

5.3.1. Calculation of Compressible Granular Filling Material Energy Absorbed

Equation (13) shows the calculation formula for $W_{compress}$:

$$W_{\text{compress}} = W'_{fe} + W'_{fc} = \int \Delta F \times S = \int (F_u - F_d) \times S \tag{13}$$

where ΔF is the load loss value; F_d is the load on the secondary lining, which is the loading force on the top of the supported beam in the test; F_u is the load generated by the deformation of surrounding rock, which is the pressure on the pressure sensor at the bottom of the supported beam in the test; and S is the deformation displacement of surrounding rock, which is the compression amount of the granular material in the test.

According to Equation (13) and test data, the energy absorbed by each compressible granular filling material is calculated and shown in Figure 26.

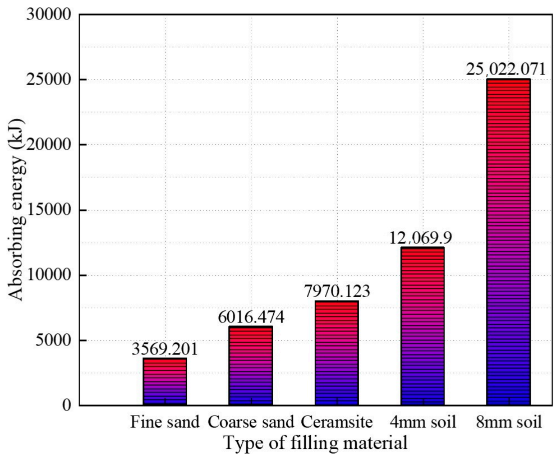

Figure 26. Energy absorption diagram of each filling material.

As shown in Figure 26, the order of the energy absorption value of the compressible granular filling material is fine sand < coarse sand < ceramsite < 4 mm soil < 8 mm soil. It is proven that 8 mm soil can satisfactorily absorb the force exerted by the surrounding rock. It can also reduce the force exerted by the secondary lining support to ensure the stability of the secondary lining support structure.

5.3.2. Calculation of the Discharge and Energy Release of Compressible Granular Filling Material

The pressure relief effect of the granular material filling the lining support is analyzed from an energy perspective. W_{unload} is equal to the difference value between the product of the deflection of the supported beam and the corresponding load before and after sand unloading. The theoretical calculation process is as follows:

The bending moment of the steel channel beam at any point under uniform load q is:

$$M(x) = \frac{qlx}{2} - \frac{qx^2}{2} = \frac{q(lx - x^2)}{2} \tag{14}$$

where *M(x)* denotes the bending moment at x from the end of the beam; q denotes the uniform load acting on the beam after homogenization of the granular filling, and l represents the length of the beam.

Then, the approximate differential equation for the deflection curve is:

$$EIw'' = -M(x) = -\frac{qlx}{2} + \frac{qx^2}{2} \tag{15}$$

where E denotes the elastic modulus of the steel beam, I denotes the moment of inertia of the channel, and w indicates the deflection of the beam.

The deflection equation is obtained by integrating the bending moment equation twice:

$$EIw = \int (-M(x)dx)dx + Ax + B = -\frac{qlx^3}{12} + \frac{qx^4}{24} + Ax + B \tag{16}$$

where A and B denote constants.

Using boundary conditions:

$$w = 0 \text{ when } x = 0,\ x = l,$$

Solution $A = \frac{ql^3}{24}$, $B = 0$.

Then, the deflection curve equation of the supported beam under uniform load is:

$$w(x) = \frac{qx(x^3 - 2lx^2 + l^3)}{24EI} \tag{17}$$

It can be seen from the test that when the compressible granular fillings are discharged, the uniform load q decreases with the change in time t. Assuming that the load before discharge is q_0 and the load after discharge is $q(t)$, then the energy W_{unload} released by compressible granular fillings is unloaded as follows:

$$W_{unload} = W'_{f\,c} = \int_0^l (q_0 - q(t))w(x)dx \tag{18}$$

Substituting it into Equation (17), Equation (18) is

$$\frac{(q_0 - q(t))^2}{24EI}\left(\frac{x^5}{5} - \frac{lx^4}{2} + \frac{l^3x^2}{2}\right)_0^l = \frac{(q_0 - q(t))^2 l^5}{120EI}$$

The pressure value measured in the test is transformed into a uniform load. The energy discharge value of the compressible granular filling material unloading process can be determined using the theoretical calculation Equation (18), according to the difference between the loading force at the top and the pressure at the bottom of the supported beam as measured in the test. This is multiplied by the settlement value caused by the discharge of compressible granular filling material. The energy discharge value in the test process was calculated. Finally, the energy discharge value calculated theoretically and the energy discharge value measured by test were compared and analyzed, as shown in Figure 27.

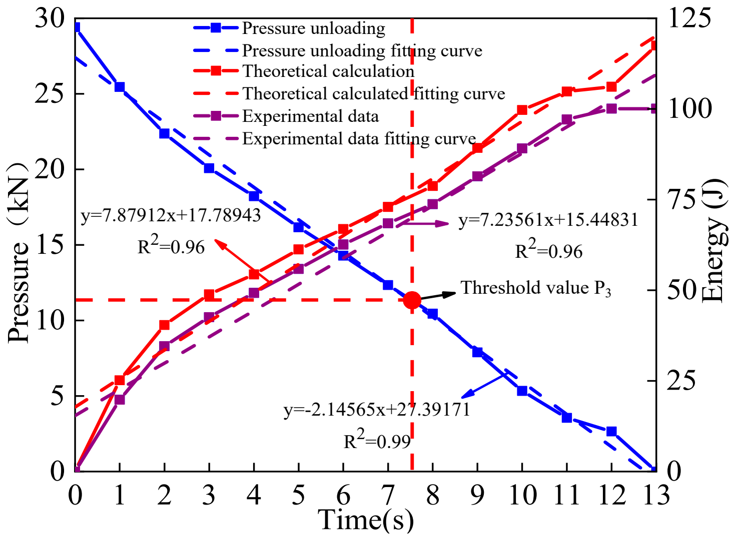

Figure 27. Diagram of the unloading pressure and energy release of the sand-filled lining.

As seen in Figure 27, with increasing sand discharge time, the pressure at the bottom of the supported beam shows a linear decline trend. In addition, the released energy shows an increasing linear trend. The pressure relief rate at the bottom of the compressible granular filling material decreases first and then rises. The reason is that the compressive compactness of sand is the largest. The friction force is also the largest when the sand first starts to unload. The pressure relief rate in the early stage is generally low, and more sand is discharged when the pressure relief valve has just been opened. With the sand filling the pressure relief valve, the pressure relief rate decreases, so the pressure relief rate in the first 4 s shows a downward trend. As more sand escapes from the supported beam, the sand compactness and friction begin to decrease. The rate of relief pressure increases, so it shows an increasing trend.

When the bottom pressure of the granular filling material reaches the set threshold value P_3, the pressure relief valve closes, the compressible granular sand stops discharging, and the support structure pressure is maintained at P_3 without further increase. If the threshold value of the pressure relief valve is lowered, the compressible granular material will continue to discharge until the pressure at the bottom drops to zero. The granular material completely discharges. The results show that the granular material filling the lining can unload the load on the lining structure by compression absorption and discharge release of the granular material.

The theoretically calculated data and the experimental data of the unloading release energy have the same trend. The theoretically calculated data are slightly higher than the experimental data. The main reason is that there were energy losses during the experiment due to, for example, friction energy consumption between particles. This is in addition to energy consumption in the opening of the pressure relief valve, and energy consumption in the conversion of kinetic and thermal energy. Theoretical calculations are loss-free. Through the test and theoretical analysis, it is proven that yielding-pressure and relief-pressure support technology that can form a controllable surface support force through compression and discharge of compressible granular filling material is a feasible support concept.

6. Conclusions

Given the structural stress characteristics of a high ground-stress soft-rock tunnel lining, an experimental study of yielding-pressure and relief-pressure support of granular material-filled lining was carried out. The conclusions are described below.

(1) From the analysis of the confined compressive strain law, it is concluded that the final compressive strain of 8 mm soil is the highest. This can provide the maximum compression deformation space and approximately 50% of the compression space. The following conclusions are drawn from the law of load reduction: 8 mm soil has the highest load reduction effect, and its maximum load reduction rate can reach 71%.

(2) By analyzing the test of a sand-filled simply supported beam, it is concluded that the maximum reduction rate of deflection of sand-filled lining is 36.7%, and the maximum reduction rate of pressure is 78%. Through the analysis of the energy released by the sand-filled lining, it is concluded that the discharge of granular material can unload the load of surrounding rock applied to the secondary lining structure and release energy. This dramatically reduces the damage to the secondary lining caused by the surrounding rock.

(3) The granular material-filled lining support can provide uniform and controllable surface support force. It can also reduce stress concentration, homogenize surrounding rock pressure, and avoid excessive development of the plastic zone. It can also achieve a better yielding-pressure effect. By discharging particles, the partial pressure of the surrounding rock is unloaded, resulting in better relief-pressure performance. The uncontrollable deformation of the tunnel's surrounding rock is transformed into a controllable state. This reduces the stress in the surrounding rock behind the lining and ensures the long-term service of the lining structure in a lower-stress surrounding-rock environment.

(4) The difference between this study and previous studies is that the innovative support method of granular-filled lining yielding and relief pressure is proposed, which

can not only improve the stability of surrounding rock by yielding- and relief-pressure effects but also reduce the damage of surrounding rock to the secondary lining structure so that the force of the support system tends to be more reasonable. This support method is more adaptable to high ground-stress soft rock. This research offers innovative prospects for improving tunnel stability and provides a better design idea for tunnel support.

Future work: Strain rate or loading rate is a key parameter that affects the strength and deformation response of granular and bound materials such as natural soils, rocks, and cemented soils [44]. This aspect was not properly considered in the present study, and the authors will consider the effect of strain/loading rate on the deformation behavior of the lining and also consider the study of incorporating the loading rate of different geomaterials [45–48]. The above sections will serve as the authors' future research work.

Author Contributions: Formal analysis, J.L. (Jie Liu) and B.W.; carrying out experiments, X.X. and J.L. (Jun Lan); data curation, Y.W. and L.S.; writing—original draft preparation, J.L. (Jie Liu) and B.W.; writing—review and editing, J.L. (Jie Liu) and B.W. All authors have read and agreed to the published version of the manuscript.

Funding: This work was supported by the National Natural Science Foundation of China (No. 52079071) and the Key Projects of National Natural Science Foundation of China (51439003).

Institutional Review Board Statement: Not applicable.

Informed Consent Statement: Not applicable.

Data Availability Statement: All data generated or analyzed during this study are included in this published article.

Conflicts of Interest: The authors declare no conflict of interest.

References

1. Kang, H.; Wang, J.; Lin, J. High-prestressed robust support system and its application in deep roadway. *J. China Coal Soc.* **2007**, *35*, 1233–1238.
2. Zhou, Y.; He, C.; Wang, B.; Zou, Y. Research on deformation control technology of soft rock tunnel in strong earthquake zone based on support parameter optimization. *Geotech. Mech.* **2013**, *34*, 1147–1155. [CrossRef]
3. Xie, S.; Xie, G.; He, S.; Zhang, G.; Yang, J.; Li, E.; Sun, Y. The support mechanism of deep soft rock roadway reinforced by shotcrete and bolt injection and its application. *J. China Coal Soc.* **2014**, *39*, 404–409. [CrossRef]
4. Liu, Z.; Li, W.; Sun, M.; Zhu, Y. Comprehensive monitoring and measurement analysis of the F4 fault section of Wushaoling Tunnel. *Chin. J. Rock Mech. Eng.* **2006**, *25*, 1502–1511.
5. Li, T. Construction control technology of soft rock with high in-situ stress and large deformation in the maoyushan tunnel. *Mod. Tunn. Technol.* **2011**, *48*, 59–67. [CrossRef]
6. Liu, G.; Zhang, F.; Li, X.; Yang, C. Characteristics and mechanism analysis of large deformation of Muzhailing tunnel. *Chin. J. Rock Mech. Eng.* **2005**, *24*, 5521–5526.
7. Qiu, W.; Wang, G.; Gong, L.; Shen, Z.; Li, C.; Dang, J. Develop and apply of an energy-limited support structure with limited resistance to adapt to large tunnel deformation. *J. Rock Mech. Eng.* **2018**, *37*, 1785–1795. [CrossRef]
8. Wang, J.; Hu, Y.; Liu, Z. Principles of Compression-type Deformation and Extensibility Support for the tunnel in soft surrounding Rock with high ground Stress. *Mod. Tunn. Technol.* **2012**, *49*, 9–17. [CrossRef]
9. Hu, X.; He, C.; Yang, Q.; Cao, S. Model test study on supporting structure type of segment-based lining combined with ceramsite compressible layer. *China Civ. Eng. J.* **2017**, *50*, 111–121. [CrossRef]
10. Hu, X.; He, C.; Yang, Q.; Wu, D. Interaction model between supporting structure and surrounding rock of segment lining and ceramsite compressible layer. *Eng. Mech.* **2018**, *35*, 86–95.
11. Yang, F. Research on Deformation and Failure Character and Yielding Support Mechanism in High Stress Soft Rock Roadway. Ph.D. Thesis, China University of Mining and Technology, Xuzhou, China, 2007.
12. Xu, G.; He, C.; Yang, Q.; Wang, B. Progressive failure process of secondary lining of a tunnel under creep effect of surrounding rock. *Tunn. Undergr. Space Technol.* **2019**, *90*, 76–98. [CrossRef]
13. Xu, G.; He, C.; Chen, Z.; Yang, Q. Transversely isotropic creep behavior of phyllite and its influence on the long-term safety of the secondary lining of tunnels. *Eng. Geol.* **2020**, *278*, 105834. [CrossRef]
14. Xu, G.; Gutierrez, M. Study on the damage evolution in secondary tunnel lining under the combined actions of corrosion degradation of preliminary support and creep deformation of surrounding rock. *Transp. Geotech.* **2021**, *27*, 100501. [CrossRef]
15. Hoek, E.; Guevara, R. Overcoming squeezing in the Yacambú-Quibor tunnel, Venezuela. *Rock Mech. Rock Eng.* **2009**, *42*, 389–418. [CrossRef]

16. Schubert, W. Dealing with squeezing conditions in Alpine tunnels. *Rock Mech. Rock Eng.* **1996**, *29*, 145–153. [CrossRef]
17. Anagnostou, G.; Cantieni, L. Design and analysis of yielding support in squeezing ground. In Proceedings of the 11th ISRM International Congress of Rock Mechanics, Lisbon, Portugal, 9–13 July 2007.
18. Wang, B.; Wang, J.; Wu, D.; Xu, J.; Zhao, Y. Discussion on applying yielding support technology for large deformation of soft-rock Tunnel. *J. Highw. Transp. Res. Dev. (Engl. Ed.)* **2015**, *9*, 69–77. [CrossRef]
19. Schubert, W. Design of ductile tunnel linings. In Proceedings of the 42nd US Rock Mechanics Symposium (USRMS), San Francisco, CA, USA, 29 June–2 July 2008.
20. Schubert, W.; Brunnegger, S.; Staudacher, R.; Wenger, J. Further development of yielding elements and connecting elements for shotcrete. *Geomech. Tunn.* **2018**, *11*, 575–581. [CrossRef]
21. Sun, J. *Theory and Practice of Underground Engineering Design*; Shanghai Science and Technology Press: Shanghai, China, 1996.
22. Varden, R.; Lachenicht, R.; Player, J. Development and Implementation of the Garford Dynamic Bolt at the Kanowna Belle Mine. In Proceedings of the Tenth AusIMM Underground Operators' Conference 2008—"Boom and Beyond" Proceedings, Launceston, TAS, Australian, 14–16 April 2008; pp. 95–102.
23. He, M.; Guo, Z. Mechanical characteristics and engineering application of rock bolts with constant resistance and large deformation. *Chin. J. Rock Mech. Eng.* **2014**, *33*, 1297–1308. [CrossRef]
24. Zhang, B.; Zhang, Z.; Wang, B.; Zhou, L. Experimental study on applying compression bolt to support large deformation tunnel. *Rock Soil Mech.* **2016**, *37*, 2047–2055. [CrossRef]
25. Li, X.; Wang, C.; Wang, H.; Diao, B. Experimental study on bearing characteristics of U-shaped steel closed definable steel frame. *J. Zhejiang Univ. (Eng. Sci.)* **2017**, *51*, 2355–2364.
26. Wu, X.; Jiang, Y.; Wang, G.; Gong, B.; Guan, Z.; Deng, T. Performance of a new yielding rock bolt under pull and shear loading conditions. *Rock Mech. Eng.* **2019**, *52*, 3401–3412. [CrossRef]
27. Zhang, C.; Lv, H.; Liu, X.; Zhou, H.; Gao, Y.; Yan, D. Study the working mechanism of a new type of constant resistance pressure relief device in a tunnel. *Rock Soil Mech.* **2020**, 1–9. [CrossRef]
28. Chen, W.; Tian, H.; Yang, F.; Geng, Y. Study the Influence of foamed concrete Reserved deformation layer the on long-term stability of Deep buried soft Rock Tunnel. *Rock Soil Mech.* **2011**, *32*, 2577–2583. [CrossRef]
29. Barla, G.; Bonini, M.L.; Semeraro, M. Analysis of the behavior of a yield-control support system in squeezing rock. *Tunn. Undergr. Space Technol.* **2011**, *26*, 146–154. [CrossRef]
30. Tian, Y.; Chen, W.; Tian, H.; Zhao, M.; Zeng, C. Research on cushion compression support design considering the strength aging weakening of soft rock. *Rock Soil Mech.* **2020**, *41*, 237–245. [CrossRef]
31. Wu, K.; Shao, Z.; Qin, S. A solution for squeezing deformation control in tunnels using foamed concrete: A review. *Constr. Build. Mater.* **2020**, *257*, 119539. [CrossRef]
32. Zheng, P.; Chen, W.; Tan, X.; Dai, Y. Study on floor heave failure mechanism and supporting technology of large deformation roadway in soft rock. *Chin. J. Rock Mech. Eng.* **2015**, *34*, 3143–3150. [CrossRef]
33. Li, Y.; Wang, X. Numerical simulation of the effect of tunnel design parameters on the surrounding rock stability. *J. Appl. Math.* **2015**, *2015*, 730672. [CrossRef]
34. Zhao, Z.; Zhang, L.; Yang, Y.; Wang, D. Numerical simulation of the influence of tunnel lining on the surrounding rock displacement field in weakly cohesive soils. *Tunn. Undergr. Space Technol.* **2018**, *81*, 131–142.
35. Niu, Y.; Xu, W.; Zhang, Q.; Li, X. Numerical simulation study on the stability of surrounding rock and optimate design of supporting structure for shield tunnel. *Adv. Civ. Eng.* **2020**, *2020*, 8835305. [CrossRef]
36. Liu, H.; Zhang, Z.; Wang, J.; Zhang, J. Numerical simulation of deformation and failure mechanism of excavation damaged zone under different tunnel lining conditions. *Adv. Civ. Eng.* **2021**, *2021*, 1–14.
37. Zhang, Q.; Xie, L.; Liu, Y.; Zuo, W.; Yang, H. Experimental investigation on the application of cushion layer for deformation control between secondary lining and surrounding rock in underground engineering. *J. Rock Mech. Geotech. Eng.* **2020**, *12*, 67–78.
38. Yang, J.; Bai, X. Application of nonlinear compressive stress-strain relationship for compacted loess in foundation settlement calculation. *Geotech. Mech.* **2015**, *36*, 1002–1008. [CrossRef]
39. Peng, Z.; Wang, L.; Jiang, Y. Measurement and Analysis of the static friction Coefficient at the interface between Particulate matter and Solids. *J. Shandong Univ. (Sci. Ed.)* **2011**, *46*, 42–45.
40. Feng, J.; Lu, H.; Wang, C. Application of M. M. Promojiyfakonov theory to solution of distance between anti-slide piles. *China Railw. Sci.* **2003**, *24*, 79–81.
41. Chang, B. A study on soil arch between stabilizing piles and critical span. In *Proceedings of the Landslides (Volume Thirteen)*; China Railway Press: Beijing, China, 1998; pp. 73–78.
42. Jiang, L.; Huang, R.; Jiang, Z. Calculation of soil arch effect between piles and analysis of pile spacing in clayey soil. *Geotechnics* **2006**, *27*, 445–450. [CrossRef]
43. Lei, S.; Zhao, W. Research the ring pressure support mechanism of large deformation in soft rock tunnels. *J. Rock Mech.* **2020**, *41*, 1039–1047. [CrossRef]
44. Maqsood, Z.; Koseki, J.; Kyokawa, H. Effects of loading rate on strength and deformation characteristics of gypsum mixed sand. *E3S Web Conf.* **2019**, *92*, 05008. [CrossRef]
45. Maqsood, Z.; Koseki, J.; Ahsan, M.K.; Shaikh, M.; Kyokawa, H. Experimental study on hardening characteristics and loading rate dependent mechanical behaviour of gypsum mixed sand. *Constr. Build. Mater.* **2020**, *262*, 119992. [CrossRef]

46. Maqsood, Z.; Koseki, J.; Miyashita, Y.; Xie, J.; Kyokawa, H. Experimental study on the mechanical behaviour of bounded geomaterials under creep and cyclic loading considering effects of instantaneous strain rates. *Eng. Geol.* **2020**, *276*, 105774. [CrossRef]
47. Augustesen, A.; Liingaard, M.; Lade, P.V. Evaluation of time-dependent behavior of soils. *Int. J. Geomech.* **2004**, *4*, 137–156. [CrossRef]
48. Enomoto, T.; Koseki, J.; Tatsuoka, F.; Sato, T. Rate-dependent behaviour of undisturbed gravelly soil. *Soils Found.* **2016**, *56*, 547–558. [CrossRef]